

論文 / 著書情報
Article / Book Information

Title	Temporal magnetotellurics reveals mechanics of the 2012 Mount Tongariro, NZ, eruption
Authors	Graham J. Hill, Hugh M. Bibby, Jared Peacock, Erin L. Wallin, Yasuo Ogawa, Luca Caricchi, Harry Keys, Stewart L. Bennie, Yann Avram
Citation	Geophysical Research Letters, vol. 47, no. 8,
Pub. date	2020, 4
DOI	https://doi.org/10.1029/2019GL086429
Creative Commons	Information is in the article.

Geophysical Research Letters

RESEARCH LETTER

10.1029/2019GL086429

Key Points:

- We identify significant temporal change in preeruption and posteruption magnetotelluric soundings
- An eruption mechanism model is developed consistent with both geophysical and geological observations
- Magnetotellurics is a viable additional monitoring tool for active volcanic systems

Supporting Information:

- Supporting Information S1

Correspondence to:

G. J. Hill,
gjhill@ig.cas.cz

Citation:

Hill, G. J., Bibby, H. M., Peacock, J., Wallin, E. L., Ogawa, Y., Caricchi, L., et al. (2020). Temporal magnetotellurics reveals mechanics of the 2012 Mount Tongariro, NZ, eruption. *Geophysical Research Letters*, 47, e2019GL086429. <https://doi.org/10.1029/2019GL086429>

Received 27 NOV 2019

Accepted 8 APR 2020

Accepted article online 17 APR 2020

© 2020. The Authors.

This is an open access article under the terms of the Creative Commons Attribution-NonCommercial License, which permits use, distribution and reproduction in any medium, provided the original work is properly cited and is not used for commercial purposes.

Temporal Magnetotellurics Reveals Mechanics of the 2012 Mount Tongariro, NZ, Eruption

Graham J. Hill^{1,2} , Hugh M. Bibby³, Jared Peacock⁴ , Erin L. Wallin⁵, Yasuo Ogawa⁶ , Luca Caricchi⁷ , Harry Keys⁸, Stewart L. Bennie³ , and Yann Avram⁹

¹Institute of Geophysics, Czech Academy of Sciences, Prague, Czech Republic, ²Gateway Antarctica, University of Canterbury, Christchurch, New Zealand, ³GNS Science, Lower Hutt, New Zealand, ⁴United States Geological Survey, Menlo Park, CA, USA, ⁵United States Army Corps of Engineers, Huntsville, AL, USA, ⁶Volcanic Fluid Research Centre, Tokyo Institute of Technology, Tokyo, Japan, ⁷Department of Earth Sciences, University of Geneva, Geneva, Switzerland, ⁸Department of Conservation, Turangi, New Zealand, ⁹Phoenix Geophysics, Toronto, Ontario, Canada

Abstract Monitoring dynamics of volcanic eruptions with geophysics is challenging. In August and November 2012, two small eruptions from Mount Tongariro provided a unique opportunity to image subsurface changes caused by the eruptions. A detailed magnetotelluric survey of the Tongariro volcanic complex completed prior to the eruption (2008–2010) provides the preeruption structure of the magmatic system. A subset of the initial measurement locations was reoccupied in June 2013. Significant changes were observed in phase tensor data at sites close to the eruptive center. Although subsurface electrical resistivity changed, the geometry of the preeruptive reservoir did not. These subsurface resistivity variations are interpreted as being predominantly caused by interaction of partial melt and the overlying brine layer causing volume reduction of the brine layer through phreatic eruption. The ability to detect significant changes associated with the magma reservoir suggests that magnetotellurics can be a valuable volcano monitoring tool.

Plain Language Summary Preeruption and posteruption electromagnetic magnetotelluric measurements are used to determine the variation in subsurface electrical properties resulting from changes in the Tongariro volcanic center magma chamber associated with the 2012 eruptive cycle. The observed electrical property changes are related to the physical eruption properties (e.g., eruptive volume, style, and composition), revealing the state of the magmatic system both prior to and following the eruption. Knowing both the preeruption and posteruption states of the magmatic system and the surface eruptive properties enables reconstruction of the subsurface eruption mechanism. Successful identification of preeruption and posteruption states of the volcano is evidence for the usefulness of continuous magnetotelluric monitoring of volcanoes to identify variations within magmatic systems that may be indicative of imminent eruption.

1. Introduction

Detecting geophysical signatures associated with active geologic events is key to understanding physical processes and hazard assessment. Understanding magma reservoirs (the main repositories for eruptible magma) requires an ability to detect changes in the magmatic system from surface measurements (Caudron et al., 2019; Sparks et al., 2019; Stix & de Moor, 2018). Magnetotellurics (MT) measures subsurface electrical properties and has been used successfully to determine the location and size of magmatic systems (e.g., Bedrosian et al., 2018; Ogawa et al., 2014; Peacock et al., 2016).

The Tongariro Volcanic Centre (TgVC) marks the southern boundary of the Taupo Volcanic Zone of New Zealand and includes (south to north) Mounts Ruapehu, Ngauruhoe, and Tongariro (Figure 1). The TgVC has predominantly erupted plagioclase-bearing, porphyritic two-pyroxene andesite (Price et al., 2012), while the Pahoka-Mangamate eruptive cycle (ca. 10 ka) produced basaltic andesite through dacite (Hobden et al., 1999; Nakagawa et al., 1998). Barometric estimates indicate a broad range of magma storage depths. While the Pahoka-Mangamate magma originates from a deep source region (28–35 km) and ascends rapidly, the more recent (~1.8 ka through to the historic 1975 eruption) eruptive products from Ngauruhoe (7–22 km) and Red Crater (4–9 km) return significantly shallower storage depths (Arpa et al., 2017).

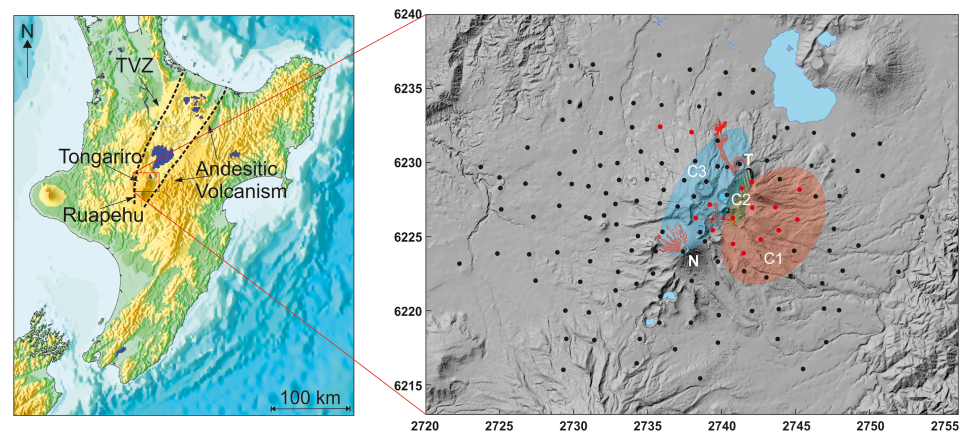


Figure 1. Magnetotelluric site locations (New Zealand Map Grid coordinate system) showing the location of the major features of the resistivity model: C1 = the reservoir (red), C2 = conduit (green), and C3 = near-surface hydrothermal system (blue), also shown in Figure 3a. Seismic activity preceding the 2012 eruptions was located within the crosshatched black ellipsoid. Both the original preeruption survey (black) and repeated posteruption (red) locations are shown. Extrusive lava flows from the Te Mari (T) and Ngauruhoe (N) vents are also shown. The left panel shows the survey area relative to the major andesitic volcanic cones of the southern Taupo Volcanic Zone.

Mount Tongariro entered a period of increased activity marked by the onset of seismicity in July 2012 (Hurst et al., 2014) followed by two small eruptions on 6 August ($<1.0 \times 10^{-3} \text{ km}^3$ material ejected) and on 21 November 2012 from the lower Te Maari crater vent (Pardo et al., 2014). The fallout products of the 21 November eruption covers an area up to 500 m in diameter (typically $<300 \text{ m}$) and composed largely of small pyroclastic density currents with a mean deposition thickness of $<1 \text{ cm}$. The maximum volume of ejected material is between 5.0×10^{-7} and $2.0 \times 10^{-6} \text{ km}^3$. Analysis of the ashfall indicates that no juvenile component was erupted; however, magmatic gas emission increased before the event and was elevated during the explosive events (Cronin et al., 2014).

A detailed preeruption MT survey (Hill et al., 2015) identified the location, extent, and electrical properties of the Tongariro magma reservoir prior to the 2012 eruptions. Data collection began in 2008 and was completed in 2010, with ~ 100 of the 136 sites collected in 2010 ~ 18 months prior to the onset of seismicity preceding the 2012 eruptions. Modeling of these data identified three major low-resistivity features that make up the magmatic and hydrothermal system of Tongariro; C1–C3 in Figure 1 represent their surface projection. The deepest feature (~ 4 – 12 km) C1 is the reservoir of the volcanic system, which extends from Mount Ngauruhoe in the south to Te Maari crater in the north and is offset east of the Tongariro massif with the western edge underlying the axial trend of the Tongariro massif vents. C2 (~ 1 – 4 km) is an intermittently used pathway for magmatic and hydrothermal fluids and gases to transition from depth to the surface, and C3 (uppermost 1.5 km) the near-surface extent of the hydrothermal system.

Low resistivity values observed in C1 are interpreted as either a crustal zone of partial melt with a high melt fraction (Hill et al., 2015) or a lower melt fraction combined with an overlying highly saline brine (Afanasyev et al., 2018; Blundy et al., 2015). Progressive magma cooling and crystallization eventually leads to the exsolution and extraction of excess magmatic fluids (Degruyter et al., 2019; Parmigiani et al., 2017). Their upward migration and decompression may lead to the separation of a vapor and a brine phase (Kouzmanov & Pokrovski, 2012). While the vapor will be released at the surface, brines can accumulate at the depth of separation and form a lens (Afanasyev et al., 2018). Because of their extremely low resistivity, a thin lens of brine can have the same bulk properties as a large volume of melt-rich magma. This lens is only present at the top of the low-resistivity body (reservoir) at ~ 3.5 – 4.5 km depth. Our results show that the low resistivity of C1 (0.4 – $2 \text{ }\Omega\text{m}$) could result from a high preeruption melt fraction of 18 – 45% or a thin overlying brine with a much lower melt fraction of 7 – 15% (Pommier & LeTrong, 2011); melt fraction estimates use the chemical composition of the pre-2012 “typical” andesite (Price et al., 2012). While it is more realistic that the zone of partial melt is composed of pockets with varying degrees of partial melt rather than a uniform distribution within the volume, the estimated melt fraction and corresponding volume is based on bulk volume and resistivity of the magma reservoir (Christopher et al., 2015).

The magma reservoir geometry suggests that magma accumulates within the “shallow-staging” reservoir east of Tongariro. During eruption, magma migrates westward before ascending to the vents along the reservoir’s western margin. Such vertical transport is consistent with a sharp lithological or structural boundary, where the resistivity contrast is 3 orders of magnitude. Preeruption seismicity (Figure 1) was focused at a depth of ~1.5–4 km (Hurst et al., 2014) on the northwestern margin of the low-resistivity zone, consistent with fluid and gas/steam movement through the system coinciding with the locus of maximum shear stress (Hill et al., 2009).

2. Materials and Methods

Fluctuations in the Earth’s natural magnetic field induce electrical currents in the Earth. The MT method exploits these induced electrical currents to determine the resistivity structure of the crust. From measurements of horizontal surface components of the electric (\mathbf{E}) and magnetic (\mathbf{H}) fields, a transfer function or impedance tensor (Cagniard, 1953; Tikhonov, 1950) \mathbf{Z} is determined in the frequency domain, defined by relationship $\mathbf{E} = \mathbf{Z}\mathbf{H}$. Similarly, the relationship between the vertical magnetic field H_z and the horizontal magnetic field is expressed in the form of an induction vector (Parkinson, 1962) \mathbf{K} so that $-\mathbf{K} \cdot \mathbf{H} = H_z$. The impedance tensor and the induction vector are complex functions of the Earth’s resistivity (ρ or conductivity $\sigma = 1/\rho$), in which period is a proxy for depth where period (t) in seconds and skin depth (δ) in meters are related by $\delta \approx 500\sqrt{\rho t}$. The 3-D distribution of resistivity is determined using inverse modeling of these functions, analogous to seismic tomography. The diffuse nature of electromagnetic wave propagation results in resistivity boundaries/interfaces not being resolved as sharp boundaries but gradients (Kordy et al., 2016a, 2016b; Siripunvaraporn et al., 2005).

Near-surface heterogeneity (e.g., seasonal variations in the hydrologic system, changes in ground saturation levels due to dynamic weather conditions, and complex surficial geology including alteration zones and different volcanic units/structure) in the resistivity structure is common in volcanic settings and causes the electric field to be disturbed (distorted) at all frequencies (Bibby et al., 2005). This distortion can be overcome by the use of the phase tensor (Φ), which preserves the underlying regional phase information free from distortion (Booker, 2014; Caldwell et al., 2004). Large-scale variations in resistivity are recoverable from the phase rather than the amplitude of the MT response. The phase relationship intrinsic to the impedance tensor \mathbf{Z} forms a second-rank 2-D tensor defined by the matrix equation $\Phi = \mathbf{X}^{-1}\mathbf{Y}$ where $\mathbf{X} = \text{Re}(\mathbf{Z})$ and $\mathbf{Y} = \text{Im}(\mathbf{Z})$. Φ can be illustrated graphically as an ellipse with the greatest and least phase corresponding to the principal axes of the ellipse. Φ is an observational indication of the inherent electrical structure (Hill et al., 2009). For repeated measurements the phase change can be represented as a phase difference tensor (Δ), $\Delta = \Phi_{t1} - \Phi_{t2}/\sqrt{\Phi_{t1}}$ where Φ_{t1} is the preeruption phase tensor and Φ_{t2} is the posteruption phase tensor (Booker, 2014; Hill et al., 2015). As with the phase tensor the difference tensor is graphically represented as an ellipse and can be used to illustrate the physical changes to the structure of the region. Φ_{max} , an invariant property (Caldwell et al., 2004) of Φ , is used to demonstrate the change in the Φ response between the preeruption and posteruption measurements as it represents the maximum current flow direction and is most sensitive to changes in low-resistivity bodies.

A threshold is required when determining if observed changes are a result of changes to the magmatic system rather than from measurement repeatability limitations associated with instrumentation. Here we use a subset of the preeruption and posteruption soundings to compute a median error tensor (\mathbf{Z}_m) for all components of the impedance tensor where the signal-to-noise ratio was below an observable noise floor (Peacock et al., 2013). The signal-to-noise ratio threshold was estimated as 3 times the average error in the impedance tensor from the two control stations. The two control sites for data quality and measurement repeatability were chosen because they best represent preeruption data quality where changes in the MT response resulting from variations in the magmatic system should not be observed (radial distance \geq depth of expected change). A tensor can be calculated from \mathbf{Z}_m representing the noise phase tensor (Φ_e), which provides a threshold for when observed changes can be attributed to subsurface processes rather than measurement noise (Figure 2). The attenuation of the propagating electromagnetic wave is inversely proportional to resistivity; therefore, in low-resistivity settings signal-to-noise ratio is inherently reduced. To be representative of overall survey conditions Φ_e is estimated from both sites overlying the low-resistivity (i.e., increased effective noise) and the control sites (i.e., decreased effective noise).

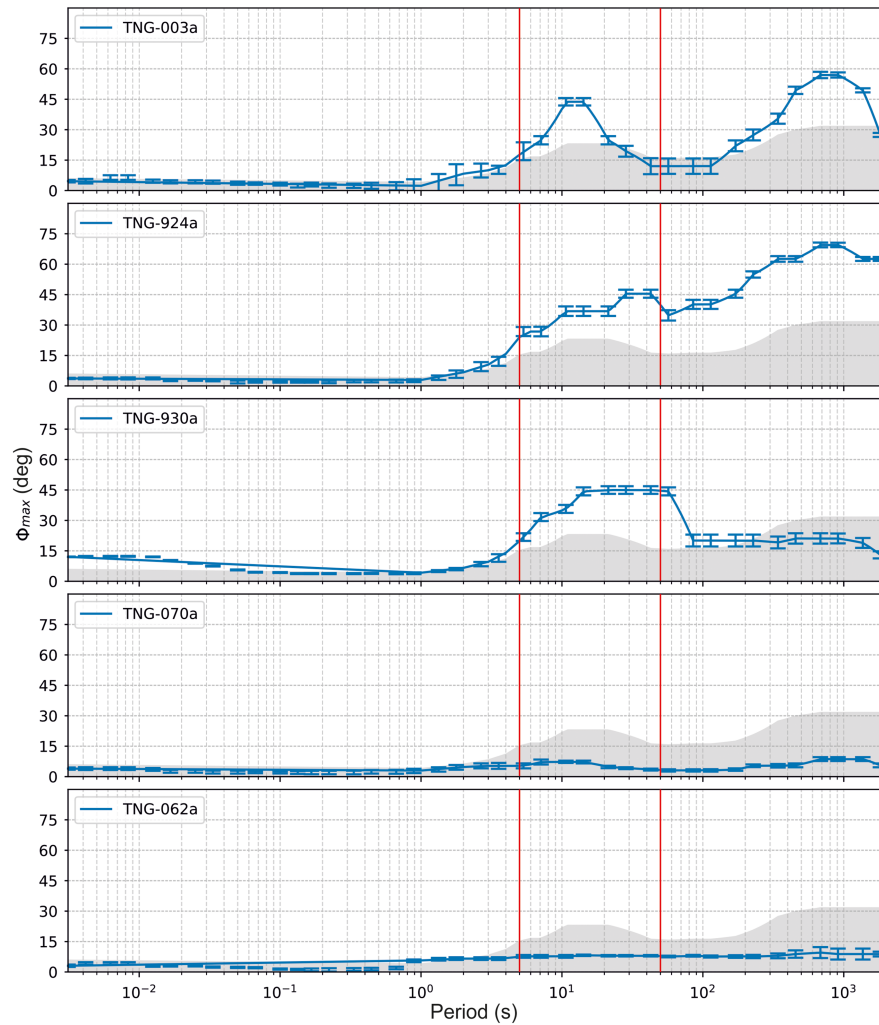


Figure 2. Plot showing the difference phase tensor property Φ_{\max} between preeruption and posteruption observations. The gray background is the estimated noise tensor difference (i.e., the change in observed response that can be attributed solely to measurement noise). The two stations distal to the eruption center (062 and 070) show no significant change. Three representative sites overlying the magmatic system (003, 924, and 930) show a clear change above the estimated error for the periods 5–50 s (red) corresponding to the \sim depth range of C1.

Posteruption reoccupation sites (Figure 1) were selected based on both the data quality of the preeruption measurements and proximity to the surface projection of the low-resistivity zone C1 (Figure 1). All repeated sites (bar the two control sites) are located within a radial distance less than the depth of the top of the reservoir where a change associated with the eruptive sequence would be expected. When possible, reoccupied locations were measured with the same instruments (9 of 16 measurements). All repeated measurements were set to reflect the original occupation as closely as possible, including use of preeruption magnetometer locations when locatable. When original magnetometer locations were not located, magnetometers were installed in the same relative orientation and within 3 m of the preeruption measurement. All posteruption electric field dipoles were set at the same length as the preeruption dipoles.

3. Results

MT responses of repeated sites were computed following the same remote robust processing approach (Jones et al., 1989) as used for the preeruption measurements. The phase of the MT response, represented by the phase tensor, is independent of near-surface temporal resistivity changes (Bibby et al., 2005). Consequently, variations between surveys may be represented by the phase difference tensor that is also independent of near-surface resistivity changes and may be represented graphically as an ellipse.

Typically, the error of the phase difference tensor is small, <1%, reaching a maximum in the period band of 5–20 s—where a change within the magmatic system is expected. The phase difference tensor for measurements overlying the magmatic system are coherent and are greater than the estimated noise phase tensor (Figure 2), suggesting they result from variations in subsurface electrical structure. The two measurements distal to the magmatic system (lower two panels in Figure 2), where little change would be expected, indeed show negligible differences. The observed measurement differences are less than the predicted noise error bounds for all periods, demonstrating that MT measurements are repeatable in a complex volcanic environment. Furthermore, no significant changes in the phase response for periods less than 1 s (representing the shallow surface structure) occur at any of the five sites shown in Figure 2. Observed changes in repeated measurements over the reservoir experience the largest changes above the noise phase tensor threshold, suggesting subsurface variations associated with magmatic activity and not measurement or instrument noise are the cause of the observed change.

The difference tensor ellipses when viewed over the entire period band observed show consistent shape, magnitude, and orientation, demonstrating that a systematic change created during the eruptive cycle has been observed (supporting information Figure S1). The Δ response for repeated sites overlying the magma reservoir is highly polarized occurring in a ~NW-SE orientation that corresponds to the direction of maximum current flow in both the preeruption and posteruption phase tensor response. The polarized nature of the observed preeruption Φ response indicates a favorable direction of current flow and suggests change within the system will be preferentially associated with the maximum phase component of the Φ response. This “current channeling” leads to the polarized nature of the Δ behavior, graphically represented by the needle-like nature of both the Φ and Δ ellipses. These observed Δ responses have a limited period band (Figures 2 and S1) with similar onset time at stations overlying the magmatic system of ~5 s, reaching a maximum observed difference at ~15 s, and return to levels that are representative of instrument and measurement noise at ~50 s. Given the resistivity dependent relationship between period and depth, onset time as used in seismic methods is not directly transferable. Changes in the integrated resistivity column observed by each station (which are expected in areas with complex 3-D structure) lead to minor variations in onset time reflecting the same feature or depth. The narrow band with significant variations in the Δ corresponds to the depth range of the magma reservoir. The systematic orientation of the Δ response and narrow period range supports the interpretation that the changes in the electrical properties result from a change within the magma reservoir that can be attributed to the eruptive cycle.

4. Discussion

Changes in electrical properties or geometry of the magma reservoir (depth ~4–10 km) are expected (based on an average of the observed resistivities overlying the magma reservoir) and observed over the period band of ~5–50 s (upper three panels of Figure 2). Figure 3 shows the observed difference tensor ellipses at two periods, 5.33 and 28.4 s. The change in phase is highly polarized with the change in orientation direction of the maximum observed preeruption phase tensors (Hill et al., 2015), a result of the extremely large resistivity contrast across the western margin of the reservoir (Figure 3). The observed narrow phase tensor difference ellipses are a result of electrical property variations in the magmatic system aligned with the direction of the original maximum phase. Observed phase tensor ellipses are narrow with the maximum produced by and orthogonal to a large change in resistivity. The orientation and shape of the best fit modeled difference ellipses result from a decrease in the maximum phase (Figure 3). However, observed difference phase tensor ellipses suggest that the posteruption phase response is still highly polarized and results from a significant (but reduced from preeruption) resistivity gradient orthogonal to the ellipse long axis (Figure 3).

Computing a full inverse model is not possible using the small reobserved data set. Instead, required changes to the preeruption model were tested using the preeruption model as the a priori starting model and computing the updated or perturbed inverse result using only the 16 posteruption measurements, with the same error, and smoothing parameters applied. There are two problems with this approach. First, by including both phase and amplitude data, small near-surface changes can have disproportionate influence. Second, the limited data distribution can be fit by changing the resistivity in regions where the model is not constrained by data. The inverse modeling was computed using WSINV3DMT (Siripunvaraporn et al., 2005) on the Tokyo Institute of Technology Supercomputer and converged after two iterations. The inversion

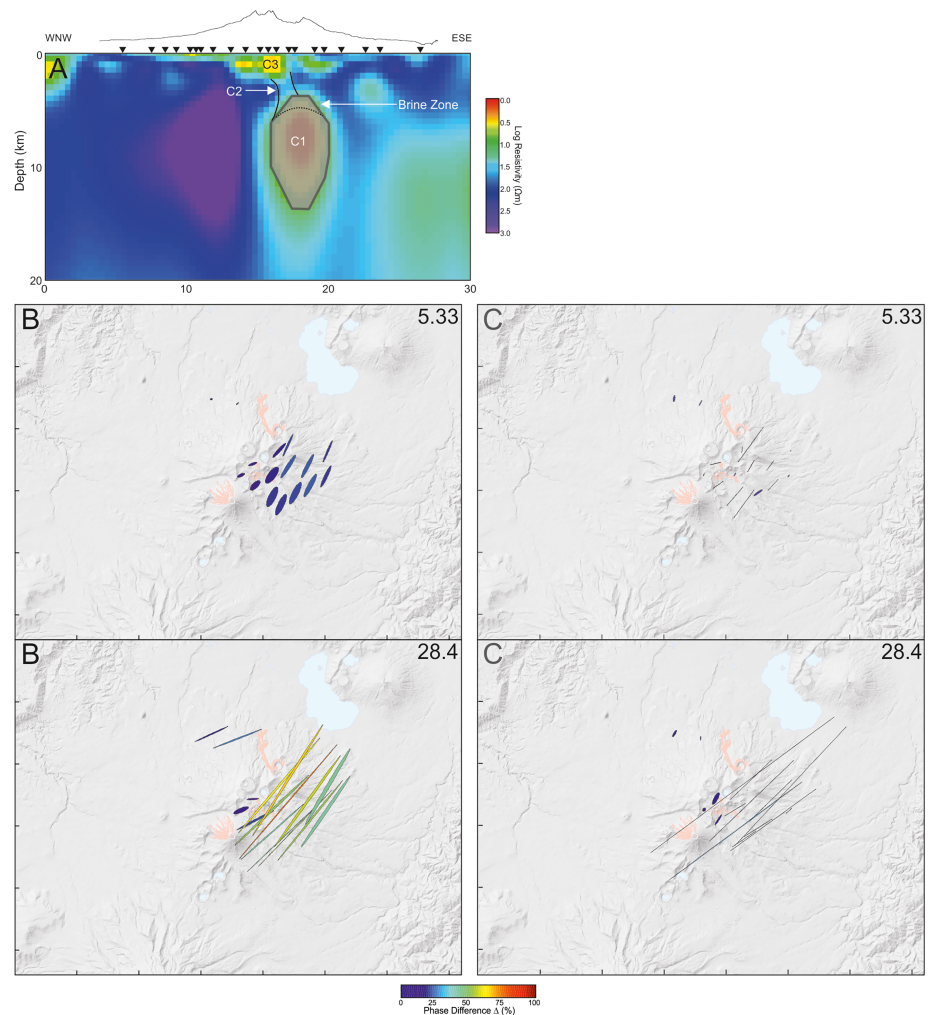


Figure 3. Difference ellipses. (a) Preeruption cross section showing the preeruption reservoir C1 where the resistivity was varied. (b) Synthetic difference ellipses when the resistivity of C1 has been increased to $15 \Omega\text{m}$ and the brine layer removed which best reproduce the magnitude and direction of the observed difference tensor. (c) Observed difference ellipses (as the change is highly polarized the ellipse minor axis is small leading to the narrow shape) at two periods (5.33 and 28.4 s) showing the first onset of differences above 7% at 5.33 s and the highly polarized (represented by the elongate ellipse) nature of the change at 28.4 s. Note difference tensor ellipses are plotted at 4 times scale of those in supporting information Figure S1.

showed an increase in resistivity near Te Maari crater and the reservoir, but lack of constraint over the wider survey area allowed the inversion algorithm to balance the increase of resistivity where there were data by decreasing the resistivity in regions where there is no posteruption data. Although it is possible to include preeruption measurements as constraints in the inverse modeling, there is no way to predetermine the extent of the resistivity change and identify which preeruption measurements can validly be included in the posteruption computation.

As an alternative approach, to reproduce observed changes in the phase tensor response, we calculated the phase difference tensors for a series of synthetic models (Mackie et al., 1994). As the measured change in the phase tensors suggests a change of electrical properties (via changing the volume of magmatic fluids present) rather than geometry and structure of the magmatic system, preeruption model boundaries were kept unchanged. The resistivity of the reservoir was varied to simulate reduction of the magmatic fluid volume within the reservoir to recreate the observed changes. The phase difference tensor shows the resistivity of the reservoir increased following the eruption. The resistivity within the reservoir region of the preeruption model (Figure 3) was increased from its preeruption values of $<1 \Omega\text{m}$, in steps to $50 \Omega\text{m}$ with and without

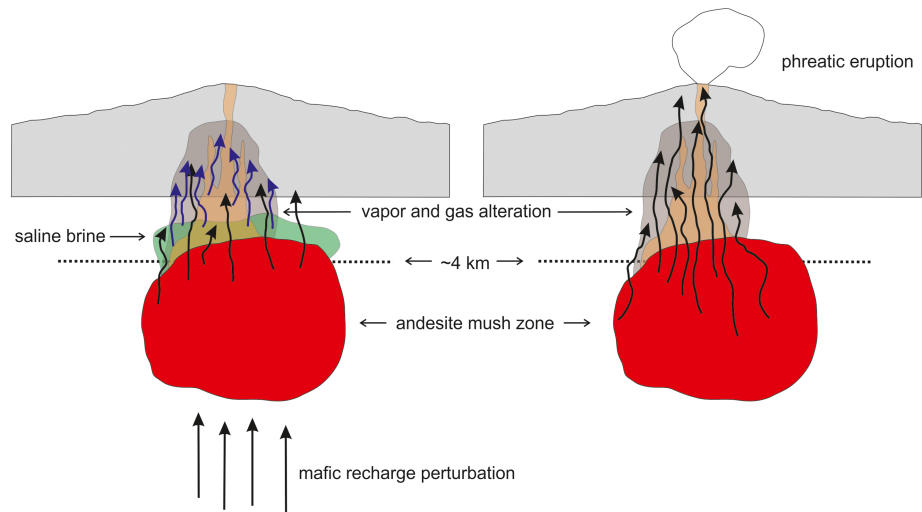


Figure 4. Preeruption and posteruption systems. The red chamber is the andesite partial melt reservoir; green the brine lens; blue arrows represent vapor (saline) coming off the brine; black arrows are gas exsolving from the magma creating the zone of alteration around the conduit (C2 in Figure 3a). Mafic recharge or an alternate perturbation of the andesite reservoir mobilizes the melt allowing it to reach the overlying brine triggering the phreatic eruption. Dashed line is ~4 km below surface.

the presence of an overlying brine lens. Best fits to size, shape, and orientation of the observed difference tensors (Figure 3) were achieved when the reservoir resistivity was increased to 15 Ωm , representing a decrease in the melt fraction of the reservoir (decreasing the resistivity gradient across the western boundary of the reservoir) and simulating the removal of the overlying brine lens (Figure 3).

If the low resistivity of the reservoir primarily results from the presence of melt, a reduction of >25% in melt fraction preeruption to posteruption is required (Pommier & LeTrong, 2011). The phase difference tensor results indicate the structure and geometry of the volcanic system did not change significantly during the eruptive phase. Based on the estimated melt component for a system where the magmatic fluids are primarily melt, the volume change associated with required reduction in partial melt fraction of the reservoir would be a minimum of $\sim 3 \text{ km}^3$, 4 orders of magnitude greater than the estimated volume of the eruptive products which did not contain a significant juvenile magmatic component (Cronin et al., 2014). Over eruptive time-scales there is potential for decompression (pressure drops of several tens of MPa) to influence the phase state of unerupted volatile-saturated magmas (Blundy & Cashman, 2001; Tuttle & Bowen, 1958), resulting in syneruptive crystallization “pressure quenching.” The syneruptive crystallization necessary to produce the $\sim 3 \text{ km}^3$ reduction melt volume would imply >65% crystallization, requiring $\sim 200 \text{ MPa}$ decompression associated with eruption (Blundy et al., 2006). This suggests that the preeruption reservoir low resistivity is not due to the presence of melt alone.

Rather, the modeled volume of preeruption low resistivity could result from a lower melt fraction zone containing pockets within the low-resistivity zone that are composed of higher melt fraction eruptible (mobile) partial melt and overlain by a thin extremely low-resistivity brine layer. The presence of a preeruption brine layer provides a mechanism for the phreatic eruptions. As magma migrated vertically through the magmatic system it encountered the brine layer at the top of the reservoir and eventual water in the hydrothermal system, triggering the phreatic eruptions and the consequent removal of this low-resistivity brine layer (Figure 4), and a small amount of melt representing juvenile material erupted. Removal of the brine during the eruption cycle coupled with a small change ($\sim 3\text{--}5\%$) in the melt fraction (Pommier & LeTrong, 2011) due to syneruptive “pressure quenching” would produce the $\sim 15 \text{ }\Omega\text{m}$ change in the bulk resistivity required in the forward modeling studies to recreate the observed difference phase tensor. The measurable change between the preeruption and posteruption data sets indicates that the phreatic eruptions resulted in a small reduction in the melt fraction and elimination of an overlying brine layer, identifying the principal mechanism and processes occurring within the magmatic system during the 2012 eruptive cycle.

Measurement stability and the ability to observe changes within the reservoir suggest that MT can be a valuable monitoring tool. Traditional volcanic monitoring using seismicity and deformation is typically sensitive to “active” processes of material moving through the magmatic system. In contrast, MT is sensitive to more “passive” processes within the magmatic system, specifically to a change in the fluid component (i.e., increase in melt and fluid fraction). As such, MT monitoring could provide useful data in cases where traditional monitoring techniques show little unrest prior to eruption (Dzurisin et al., 2008). Adding MT and additional data types to standard monitoring techniques would provide additional information sensitive to different physical properties and processes occurring prior to eruption. Continuous MT data could add useful information for understanding the dynamic nature of magmatic systems (Aizawa et al., 2011), allowing the investigation of fundamental questions, such as how quickly the melt fraction changes within the reservoir and whether there is a dynamic perturbation and remobilization of magma (Jackson et al., 2018) immediately before onset of eruptive activity.

Funding

Data acquisition for posteruption measurements were supported by GNS Science core funding (MBIE). G. H.’s time was supported by New Zealand Royal Society Marsden Award ASL-1301 and a Lumina Quarentur fellowship LQ100121901. Travel and field support for Y. O. was provided by a New Zealand Royal Society ISAT award to G. H.

Author Contributions

G. H. designed the study; G. H., H. B., E. W., S. B., and Y. O. collected the field data. G. H. carried out the time series analysis, G. H. and J. P. the repeatability phase tensor analysis, and G. H. and Y. O. the inverse and forward computations, and HK determined the 21 November eruption volume estimate. G. H. wrote the initial draft, and all authors contributed to the interpretation and final manuscript preparation.

Data and Materials Availability

Data used in this study are available from the USGS data center (<https://doi.org/10.5066/P9B1XU7O>).

Acknowledgments

Initial motivation for the study stemmed from discussions with Art Jolly (GNS Science). We thank Tony Orr (Helisika) for providing helicopter support making sure everyone got off the mountain each day, and are grateful to Alistair Pearce for his company and assistance in the field during collection of repeat measurements. We thank Christian Huber for editorial handling, and the comments of two anonymous reviewers and Branden Dean which improved the clarity of the manuscript. Any use of trade, firm, or product names is for descriptive purposes only and does not imply endorsement by the U.S. Government.

References

- Afanasyev, A., Blundy, J., Melnik, O., & Sparks, S. (2018). Formation of magmatic brine lenses via focused fluid-flow beneath volcanoes. *Earth and Planetary Science Letters*, *486*, 119–128. <https://doi.org/10.1016/j.epsl.2018.01.013>
- Aizawa, K., Kanda, W., Ogawa, Y., Iguchi, M., Yokoo, A., Yakiwara, H., & Sugano, T. (2011). Temporal changes in electrical resistivity at Sakurajima volcano from continuous magnetotelluric observations. *Journal of Volcanology and Geothermal Research*, *199*, 165–175.
- Arpa, M. C., Zellmer, G. F., Christenson, B., Lube, G., & Shellnutt, G. (2017). Variable magma reservoir depths for Tongariro volcanic complex eruptive deposits from 10,000 years to present. *Bulletin of Volcanology*, *79*(7). <https://doi.org/10.1007/s00445-017-1137-5>
- Bedrosian, P. A., Peacock, J. R., Bowles-Martinez, E., Schultz, A., & Hill, G. J. (2018). Crustal inheritance and a top-down control on arc magmatism at Mount St Helens. *Nature Geoscience*, *11*(11), 865–870. <https://doi.org/10.1038/s41561-018-0217-2>
- Bibby, H. M., Caldwell, T. G., & Brown, C. (2005). Determinable and non-determinable parameters of galvanic distortion in magnetotellurics. *Geophysical Journal International*, *163*, 915–930.
- Blundy, J., & Cashman, K. (2001). Ascent-driven crystallisation of dacite magmas at Mount St Helens, 1980–1986. *Contributions to Mineralogy and Petrology*, *140*, 631–650.
- Blundy, J., Cashman, K., & Humphreys, M. (2006). Magma heating by decompression-driven crystallization beneath andesite volcanoes. *Nature*, *443*(7107), 76–80. <https://doi.org/10.1038/nature05100>
- Blundy, J., Mavrogenes, J., Tattitch, B., Sparks, R. S. J., & Gilmer, A. (2015). Generation of porphyry copper deposits by gas-brine reaction in volcanic arcs. *Nature Geoscience*, *8*, 235–240. <https://doi.org/10.1038/NGEO2351>
- Booker, J. R. (2014). The magnetotelluric phase tensor: A critical review. *Surveys in Geophysics*, *35*(1), 7–40. <https://doi.org/10.1007/s10712-013-9234-2>
- Cagniard, L. (1953). Basic theory of the magneto-telluric method of geophysical prospecting. *Geophysics*, *18*, 603–635.
- Caldwell, T. G., Bibby, H. M., & Brown, C. (2004). The magnetotelluric phase tensor. *Geophysical Journal International*, *158*, 457–469.
- Caudron, C., Girona, T., Taisne, B., Suparjan, Gunawan, H., Kristianto, & Kasbani (2019). Change in seismic attenuation as a long-term precursor of gas-driven eruptions. *Geology*, *47*(7), 632–636. <https://doi.org/10.1130/G46107.1>
- Christopher, T. E., Blundy, J., Cashman, K., Cole, P., Edmonds, M., Smith, P. J., et al. (2015). Crustal-scale degassing due to magma system destabilization and magma-gas decoupling at Soufrière Hills Volcano, Montserrat. *Geochemistry, Geophysics, Geosystems*, *16*, 2797–2811. <https://doi.org/10.1002/2015GC005791>
- Cronin, S., Stewart, C., Zernack, A., Brenna, M., Procter, J., Pardo, N., et al. (2014). Volcanic ash leachate compositions and assessment of health and agricultural hazards from 2012 hydrothermal eruptions, Tongariro, New Zealand. *Journal of Volcanology and Geothermal Research*, *286*, 233–247.
- Degruyter, W., Parmigiani, A., Huber, C., & Bachmann, O. (2019). How do volatiles escape their shallow magmatic hearth? *Philosophical Transactions of the Royal Society of London*, *377*. <https://doi.org/10.1098/rsta.2018.0017>

- Dzurisin, D., Lisowski, M., Poland, M. P., Sherrod, D. R., & LaHusen, R. G. (2008). Constraints and conundrums resulting from ground-deformation measurements made during the 2004–2005 dome-building eruption of Mount St. Helens, Washington. In D. R. Sherrod, W. E. Scott, & P. H. Stauffer (Eds.), *A volcano rekindled; the renewed eruption of Mount St. Helens, 2004–2006*, Chap. 14, (Vol. 1750, pp. 281–300). Reston, VA: United States Geological Survey.
- Hill, G. J., Bibby, H. M., Ogawa, Y., Wallin, E. L., Bennie, S. L., Caldwell, T. G., et al. (2015). Structure of the Tongariro volcanic system: Insights from magnetotelluric imaging. *Earth and Planetary Science Letters*, *432*, 115–125. <https://doi.org/10.1016/j.epsl.2015.10.003>
- Hill, G. J., Caldwell, T. G., Heise, W., Chertkoff, D. G., Bibby, H. M., Burgess, M. K., et al. (2009). Imaging magmatic systems using magnetotelluric data: Mount St. Helens and Mount Adams. *Nature Geoscience*, *2*, 785–789. <https://doi.org/10.1038/ngeo661>
- Hobden, B. J., Houghton, B. F., Davidson, J. P., & Weaver, S. D. (1999). Small and short-lived magma batches at composite volcanoes: Time windows at Tongariro volcano, New Zealand. *Journal of the Geological Society of London*, *156*, 865–868.
- Hurst, T., Jolly, A. D., & Sherburn, S. (2014). Precursory characteristics of the seismicity before the 6 August 2012 eruption of Tongariro volcano, North Island, New Zealand. *Journal of Volcanology and Geothermal Research*, *286*, 294–302. <https://doi.org/10.1016/j.jvolgeores.2014.03.004>
- Jackson, M. D., Blundy, J., & Sparks, R. S. (2018). Chemical differentiation, cold storage and remobilization of magma in the Earth's crust. *Nature*, *564*(7736), 405–409. <https://doi.org/10.1038/s41586-018-0746-2>
- Jones, A. G., Chave, A. D., Egbert, G., Auld, D., & Bahr, K. (1989). A comparison of techniques for magnetotelluric response function estimation. *Journal of Geophysical Research*, *94*, 14,201–14,213.
- Kordy, M., Wannamaker, P., Maris, V., Cherkaev, E., & Hill, G. (2016a). Three-dimensional magnetotelluric inversion using deformed hexahedral edge finite elements and direct solvers parallelized on SMP computers, part I: Forward problem and parameter jacobians. *Geophysical Journal International*, *204*, 74–93.
- Kordy, M., Wannamaker, P., Maris, V., Cherkaev, E., & Hill, G. (2016b). Three-dimensional magnetotelluric inversion using deformed hexahedral edge finite elements and direct solvers parallelized on SMP computers, part II: Direct data-space inverse solution. *Geophysical Journal International*, *204*, 94–110.
- Kouzmanov, K., & Pokrovski, G. S. (2012). Hydrothermal controls on metal distribution in porphyry Cu (-Mo-Au) systems. *Special Publication of the Society of Economic Geologists*, *16*, 573–618.
- Mackie, R. L., Smith, J. T., & Madden, T. R. (1994). Three-dimensional electromagnetic modelling using finite difference equations: The magnetotelluric example. *Radio Science*, *29*, 923–935.
- Nakagawa, M., Nairn, I. A., & Kobayashi, T. (1998). The ~10 ka multiple vent pyroclastic eruption sequence at Tongariro volcanic centre, Taupo Volcanic Zone, New Zealand. Part 2. Petrological insights into magma storage and transport during regional extension. *Journal of Volcanology and Geothermal Research*, *86*, 45–65.
- Ogawa, Y., Ichiki, M., Kanda, W., Mishina, M., & Asamori, K. (2014). Three-dimensional magnetotelluric imaging of crustal fluids and seismicity around Naruko volcano, NE Japan. *Earth, Planets and Space*, *66*(158). <https://doi.org/10.1186/s40623-014-0158-y>
- Pardo, N., Cronin, S. J., Németh, K., Brenna, M., Schipper, C. I., Breard, E., et al. (2014). Perils in distinguishing phreatic from phreato-magmatic ash; insights into the eruption mechanisms of the 6 August 2012 Mt. Tongariro eruption, New Zealand. *Journal of Volcanology and Geothermal Research*, *286*, 397–414. <https://doi.org/10.1016/j.jvolgeores.2014.05.001>
- Parkinson, W. D. (1962). The influence of continents and oceans on geomagnetic variations. *Geophysical Journal of the Royal Astronomical Society*, *6*, 441–449.
- Parmigiani, A., Degruyter, W., Leclaire, S., Huber, C., & Bachmann, O. (2017). The mechanics of shallow magma reservoir outgassing. *Geochemistry, Geophysics, Geosystems*, *18*, 2887–2905. <https://doi.org/10.1002/2017GC006912>
- Peacock, J. R., Mangan, M. T., McPhee, D., & Wannamaker, P. E. (2016). Three-dimensional electrical resistivity model of the hydrothermal system in Long Valley caldera, California, from magnetotellurics. *Geophysical Research Letters*, *43*, 7953–7962. <https://doi.org/10.1002/2016GL069263>
- Peacock, J. R., Thiel, S., Heinson, G. S., & Reid, P. (2013). Time-lapse magnetotelluric monitoring of an enhanced geothermal system. *Geophysics*, *78*, B121–B130. <https://doi.org/10.1190/geo2012-0275.1>
- Pommier, A., & LeTrong, E. (2011). "SIGMELTS": A web portal for electrical conductivity calculations in geosciences. *Computational Geosciences*, *37*(9). <https://doi.org/10.1016/j.cageo.2011.01.002>
- Price, R. C., Gamble, J. A., Smith, I. E. M., Maas, R., Waight, T., Stewart, R. B., & Woodhead, J. (2012). The anatomy of an andesite volcano: A time-stratigraphic study of andesite petrogenesis and crustal evolution at Ruapehu volcano, New Zealand. *Journal of Petroleum*, *53*(10), 2139–2189.
- Siripunvaraporn, W., Egbert, G., Lenbury, Y., & Uyeshima, M. (2005). Three-dimensional magnetotelluric: Data space method. *Physics of the Earth and Planetary Interiors*, *150*, 3–14.
- Sparks, S., Annen, C. J., Blundy, J., Cashman, K., Rust, A., & Jackson, M. D. (2019). Formation and dynamics of magma reservoirs. *Philosophical Transactions of the Royal Society of London*, *377*.
- Stix, J., & de Moor, J. M. (2018). Understanding and forecasting phreatic eruptions driven by magmatic degassing. *Earth, Planets and Space*, *70*(83). <https://doi.org/10.1186/s40623-018-0855-z>
- Tikhonov, A. N. (1950). On determining electric characteristics of the deep layers of the Earth's crust. *Doklady Akademii Nauk SSSR*, *73*, 295–297.
- Tuttle, O. F., & Bowen, N. L. (1958). Origin of granite in light of experimental studies in the system NaAlSi₃O₈-KAlSi₃O₈-SiO₂. *Geological Society of America Memoirs*, *74*, 153.